ADVANCED FUNCTIONAL MATERIALS
www.afm-journal.de

An Integrated Computational–Experimental Hierarchical Approach for the Rational Design of an IL/UiO-66 Composite Offering Infinite CO_2 Selectivity

Muhammad Zeeshan, Hasan Can Gulbalkan, Ozce Durak, Zeynep Pinar Haslak, Ugur Unal, Seda Keskin, and Alper Uzun**

Owing to the possibility of generating theoretically unlimited numbers of ionic liquid (IL)–metal-organic framework (MOF) combinations, experimental studies on IL/MOF composites for gas separation applications are mostly conducted on a trial-and-error basis. To address this problem, an integrated computational–experimental hierarchical approach is presented for selecting the best IL-MOF combination for a target gas separation application. For this purpose, UiO-66 and pyrrolidinium-based ILs are chosen as the parent MOF and IL family, respectively, and three powerful computational tools, Conductor-like Screening Model for Realistic Solvents calculations, density functional theory calculations, and grand canonical Monte Carlo simulations, are integrated to identify the most promising IL-UiO-66 combination as 1-*n*-butyl-1-methylpyrrolidinium dicyanamide/UiO-66, [BMPyrr][DCA]/UiO-66. Then, this composite is synthesized, characterized in deep detail, and tested for CO_2/N_2, CO_2/CH_4, and CH_4/N_2 separations. Results demonstrate that [BMPyrr][DCA]/UiO-66 offers an extraordinary gas separation performance, with practically infinite CO_2 and CH_4 selectivities over N_2 at 15 °C and at low pressures. The integrated hierarchical approach proposed in this work paves the way for the rational design and development of novel IL/MOF composites offering exceptional performance for any desired gas separation application.

1. Introduction

Metal-organic frameworks (MOFs) are a distinct class of 3D porous materials with significantly large accessible surface areas and pore volumes. Owing to their tunable characteristics, diverse structures of functionalized MOFs can be designed for any target application.[1] Ionic liquids (ILs), on the other hand, are molten salts made up of large organic cations paired with inorganic anions offering unique tunable physicochemical properties thanks to an almost unlimited number of possible structures.[2] The novel composite materials obtained by incorporating ILs into MOFs via a versatile and simple post-synthesis modification strategy has emerged as a promising solution for various applications, specifically for gas separations.[3]

Recent studies demonstrated that IL/MOF composites offer a broad potential in boosting the separation performance of the parent MOFs.[3a,4] This approach provides several times improvements in CO_2/CH_4, CO_2/N_2, and CH_4/N_2 selectivities, as shown in Table S1 (see the Supporting Information). For instance, the incorporation of 1-*n*-butyl-3-methylimidazolium hexafluorophosphate ([BMIM][PF_6]) into a zeolitic imidazolate framework (ZIF-8) led to an increase in the CO_2/CH_4 selectivity from 2.7 to 9 at 1 mbar.[5] Similarly, 1-ethyl-3-methylimidazolium acetate ([EMIM][Ac])/ZIF-8 composite exhibited a CO_2/N_2 selectivity of 105 at 100 mbar, significantly higher than that of the pristine ZIF-8, 6.5, at the same condition.[4b] Studies on identifying the structural factors responsible for such selectivity improvements have indicated that structures of the IL, especially its anion type, and the MOF are crucial in determining the corresponding gas uptakes and selectivities.[6] Furthermore,

M. Zeeshan, H. C. Gulbalkan, O. Durak, Z. P. Haslak, S. Keskin, A. Uzun
Department of Chemical and Biological Engineering
Koç University
Rumelifeneri Yolu, Sariyer, Istanbul 34450, Turkey
E-mail: skeskin@ku.edu.tr; auzun@ku.edu.tr

The ORCID identification number(s) for the author(s) of this article can be found under https://doi.org/10.1002/adfm.202204149.

© 2022 The Authors. Advanced Functional Materials published by Wiley-VCH GmbH. This is an open access article under the terms of the Creative Commons Attribution-NonCommercial License, which permits use, distribution and reproduction in any medium, provided the original work is properly cited and is not used for commercial purposes.

DOI: 10.1002/adfm.202204149

M. Zeeshan, O. Durak, U. Unal, S. Keskin, A. Uzun
Koç University TÜPRAŞ Energy Center (KUTEM)
Koç University
Rumelifeneri Yolu, Sariyer, Istanbul 34450, Turkey

U. Unal, A. Uzun
Koç University Surface Science and Technology Center (KUYTAM)
Koç University
Rumelifeneri Yolu, Sariyer, Istanbul 34450, Turkey

U. Unal
Department of Chemistry
Koç University
Rumelifeneri Yolu, Sariyer, Istanbul 34450, Turkey

© 2022 The Authors. Advanced Functional Materials published by Wiley-VCH GmbH

Check for updates
16163028, 2022, 35, Downloaded from https://onlinelibrary.wiley.com/doi/10.1002/adfm.202204149 by Koc University, Wiley Online Library on [27/12/2022]. See the Terms and Conditions (https://onlinelibrary.wiley.com/terms-and-conditions) on Wiley Online Library for rules of use; OA articles are governed by the applicable Creative Commons License

the improvement in the gas separation performance, especially at low pressures, is associated with the enhancements in the interactions of the desired guest molecules with the IL/MOF composites, probed by the isosteric heat of adsorption energies of gases (ΔQ_{st}).[5,7] These studies indicate that the presence of IL offers new adsorption sites, providing a higher affinity toward one of the gases, such as CO_2, while rejecting the others, such as CH_4 or N_2.[4b,5,7a] A detailed investigation of the experimental literature shows that IL-MOF pairs are generally selected based on a trial-and-error approach, and the number of possible combinations is almost limitless.[3] Thus, developing methodologies for rationally selecting the most suitable IL-MOF combination toward a target gas separation is crucial.

Here, we demonstrate a new hierarchical approach combining atomistic and molecular level calculations with an experimental assessment to rationally design an IL/MOF composite with superior CO_2 separation performance. To show the power and accuracy of this approach, we choose to work on pyrrolidinium-based ILs, as this family of ILs has not been investigated for the preparation of IL/MOF composites before.[3] On the other side, experimental studies on IL-incorporated MOF composites reported to date for adsorption-based gas separation have been limited to a few common MOFs, such as ZIF-8, CuBTC, MIL-53(Al), and MIL-101.[7a,8] However, the most thermally and chemically stable MOFs, zirconium-based MOFs, have not received much attention to prepare their composites with ILs for gas separation applications.[9] Zirconium-based MOFs have several intriguing characteristics besides having high chemical stability, including superior adsorption capacities and ease of regenerability.[10] A recent computational study on the CO_2/N_2 separation performances of 128 different zirconium-based MOFs identified the University of Oslo-66 (UiO-66) as one of the top materials with the highest CO_2/N_2 selectivity and commercial availability.[11] Therefore, investigating the CO_2 separation performance of IL-incorporated UiO-66 composites offers a broad potential. Hence, we choose to work with this MOF.

Three computational tools, Conductor-like Screening Model for Realistic Solvents (COSMO-RS) calculations, density functional theory (DFT) calculations, and grand canonical Monte Carlo (GCMC) simulations, were combined to identify the most promising pyrrolidinium IL to couple with UiO-66. The CO_2 selectivity of IL/MOF composites is determined by both the structural properties of ILs and MOFs, and their individual selectivities. However, as shown previously, the CO_2 selectivity of IL has a dominant influence on the overall selectivity of the IL/MOF composite.[3] Thus, the major aim here is to select the IL, which offers a high CO_2 selectivity when combined with UiO-66 among a large pool of available ILs. For this purpose, first, 1488 pyrrolidinium-based ILs were screened using COSMO-RS calculations to determine the ILs with high CO_2 selectivity, the selected 27 ILs were optimized by DFT calculations and then incorporated into UiO-66 by GCMC simulations to consider the effect of UiO-66 on the gas separation performance. Based on the ΔQ_{st} values obtained from GCMC simulations, the most promising IL/UiO-66 hybrid material for CO_2 separation was identified as 1-*n*-butyl-1-methylpyrrolidinium dicyanamide, [BMPyrr][DCA]/UiO-66. Next, this promising material was synthesized and characterized in deep detail. The volumetric gas adsorption tests were then performed to examine CO_2, CH_4, and N_2 adsorption of pristine UiO-66 and the newly synthesized IL-incorporated UiO-66 in a temperature range of 15–35 °C up to 1000 mbar. Results demonstrated that the [BMPyrr][DCA]/UiO-66 composite rationally designed by our integrated computational–experimental hierarchical approach sets a new adsorbent benchmark with practically infinite CO_2 and CH_4 selectivities over N_2.

2. Results and Discussion

2.1. Design and Discovery of the Best IL/UiO-66 Composite

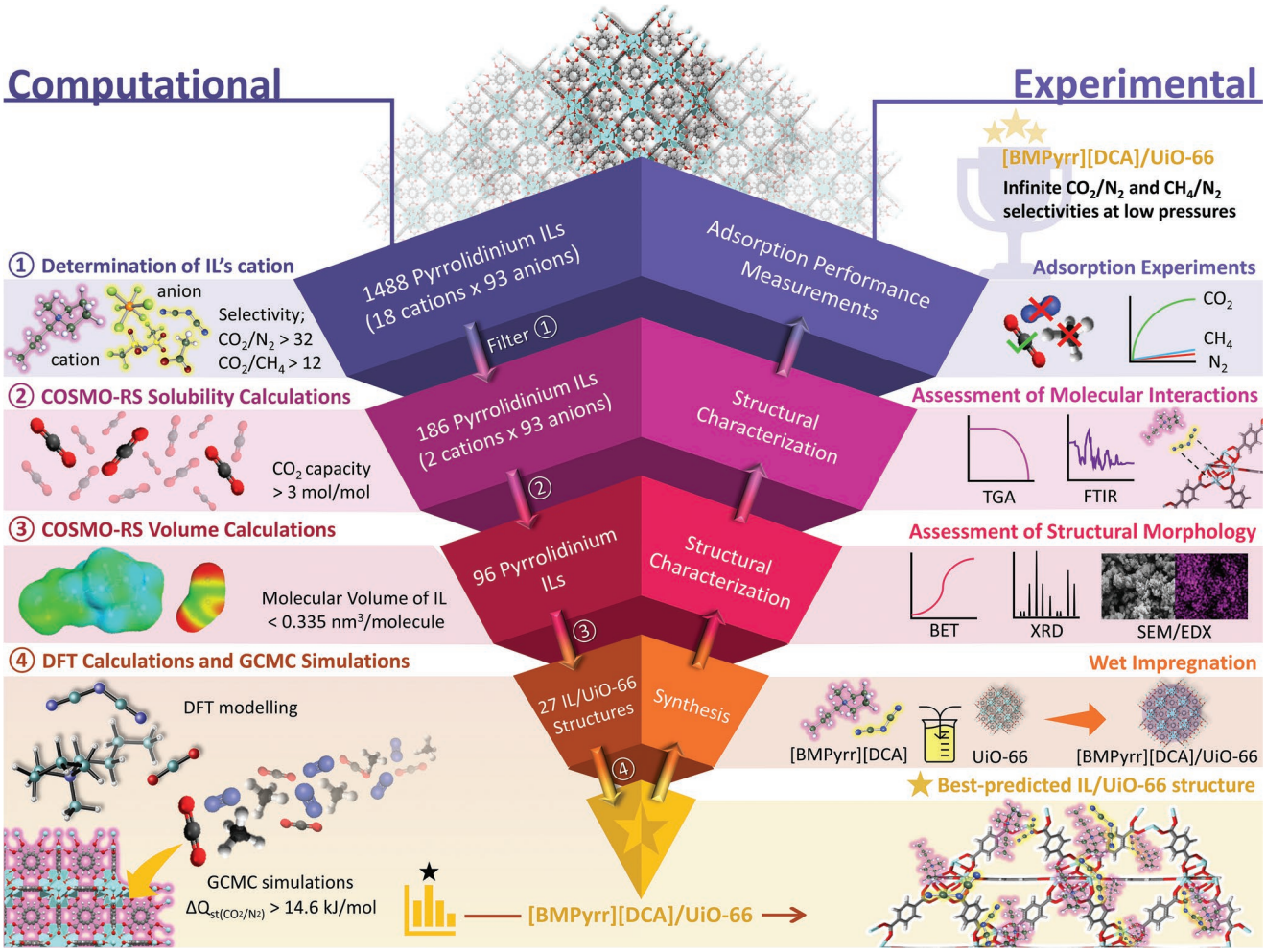
Scheme 1 represents the integrated computational–experimental hierarchical approach that we proposed for the rational design of the novel IL/MOF composites. First, COSMO-RS calculations were performed to estimate the activity coefficients at infinite dilution for CO_2, CH_4, and N_2 in a very large number of pyrrolidinium-based ILs. By using this data set, the corresponding CO_2/CH_4 and CO_2/N_2 selectivities of the bulk ILs were estimated. A total of 1488 ILs, consisting of 16 different cations and 93 different anions, were evaluated in terms of their calculated CO_2/N_2 and CO_2/CH_4 selectivities. Since the gas solubilities in ILs are mostly governed by the anion type[6a,12] (further discussion is provided in Part I of the Supporting Information), we first focused on determining the best performing cation types offering the highest CO_2/N_2 and CO_2/CH_4 selectivities, as shown in Figure S1a (Supporting Information). Accordingly, the number of cation types was narrowed down to two (1-*n*-butyl-1-methylpyrrolidinium, $[BMPyrr]^+$ and 1-(cyanomethyl)-1-methylpyrrolidinium, $[CyanoMthMPyrr]^+$) by considering ILs with CO_2/N_2 and CO_2/CH_4 selectivities higher than at least twice of the corresponding average values (15.0 and 5.6, respectively) of the entire data set. Then, using these two cations, the CO_2 separation performances of 186 ILs (corresponding to their combinations with 93 different anions present in the COSMObaseIL database (version 1501)) were examined. To further identify the top performing bulk ILs, different structures and performance filters were systematically applied. A high CO_2 solvent capacity ($C^{\infty}_{CO_2}$) is crucial to reduce the investment and energy costs,[13] and a low molecular volume is essential to ensure that a sufficient amount of IL can fit into the UiO-66. In this regard, we applied the following filters: i) $C^{\infty}_{CO_2}$>3 mol mol^{-1}, reducing the number of ILs from 186 to 96; ii) a molecular volume filter of <0.335 nm^3 per molecule, leading to a further reduction of the total number of ILs down to 27, as shown in Figure S1b (Supporting Information).

DFT calculations were performed on these 27 ILs to obtain the most stable conformer geometry for each one of them. For this purpose, a systematic conformational search was conducted at the B3LYP-D2/6-311++G** level of theory. The corresponding lowest energy equilibrium geometries obtained at the end of this step are presented in Figure S2 (Supporting Information). Then, each DFT-optimized IL was incorporated into the UiO-66 structure to generate the corresponding IL/UiO-66 composite. GCMC simulations were performed for 27 different IL/UiO-66 composites at 1000 mbar and 25 °C. Initially, the IL loading was set to ≈5 wt.%, corresponding to

© 2022 The Authors. Advanced Functional Materials published by Wiley-VCH GmbH

16163028, 2022, 35, Downloaded from https://onlinelibrary.wiley.com/doi/10.1002/adfm.202204149 by Koc University, Wiley Online Library on [27/12/2022]. See the Terms and Conditions (https://onlinelibrary.wiley.com/terms-and-conditions) on Wiley Online Library for rules of use; OA articles are governed by the applicable Creative Commons License

16163028, 2022, 35, Downloaded from https://onlinelibrary.wiley.com/doi/10.1002/adfm.202204149 by Koc University, Wiley Online Library on [27/12/2022]. See the Terms and Conditions (https://onlinelibrary.wiley.com/terms-and-conditions) on Wiley Online Library for rules of use; OA articles are governed by the applicable Creative Commons License



Scheme 1. The integrated computational-experimental hierarchical workflow leading to the IL/MOF composite offering high CO_2/N_2 and CH_4/N_2 selectivities.

12 IL ion pairs per simulation box, to examine the CO_2/N_2 separation performances of the top 27 IL/MOF composites to save from the computation cost. Previously, we showed that GCMC-calculated ΔQ_{st}, which is the difference between the isosteric heats of adsorption of gases, matched quite well with the experimental results.[5] Moreover, we observed that there is a direct relationship between ΔQ_{st} and ideal selectivity results of IL/MOF composites; ideal selectivity increases with increasing ΔQ_{st}. Therefore, by using ΔQ_{st} as a filter, the top ten IL/UiO-66 composites with the highest $\Delta Q_{st,CO_2/N_2}$ defined for a pair of CO_2 and N_2 among 27 IL/UiO-66 composites were identified according to the results obtained from GCMC simulations representing an IL loading of 5 wt.% in UiO-66, as presented in Table S2 (Supporting Information). Then, for the top ten IL/UiO-66 composites, the IL loading was increased to ≈25 wt.%, and GCMC simulations were re-performed at 1000 mbar and 25 °C. Here, an IL loading of 25 wt.% was considered, because the previous experimental reports demonstrated that the IL loading should be as high as possible to achieve the highest gas separation performance in such IL/MOF composites, and the IL loading is mostly limited to 25 wt.% in most of the MOFs before exceeding the wetness point.[14] Table S3 (Supporting Information) shows the $\Delta Q_{st,CO_2/N_2}$ values of the top ten IL/UiO-66 composites having an IL loading of ≈25 wt.%. According to the GCMC simulation results, the [BMPyrr][DCA]/UiO-66 composite exhibited the highest ΔQ_{st} value and was identified as the most promising candidate for the experimental investigation.

To complement these results, the interactions between [BMPyrr][DCA] and the gas molecules were further investigated at the DFT level. The equilibrium geometry of the [BMPyrr][DCA] was systematically optimized in the presence of CO_2, CH_4, and N_2 to identify the most favorable adsorption sites of the IL. The binding energies (BEs) of the respective IL-gas pairs were calculated for several conformations. 3D representations of the equilibrium geometries are presented in Figure S3 (Supporting Information). Calculated BEs between the IL and the gas molecules point out that [BMPyrr][DCA] has a high affinity toward CO_2 and a very low affinity for CH_4 and N_2 gases. These results support our findings based on the COSMO-RS calculations and GCMC simulations, and indicate that [BMPyrr][DCA] has a high potential for selective separation of CO_2 from CH_4 and N_2.

© 2022 The Authors. Advanced Functional Materials published by Wiley-VCH GmbH

16163028, 2022, 35, Downloaded from https://onlinelibrary.wiley.com/doi/10.1002/adfm.202204149 by Koc University, Wiley Online Library on [27/12/2022]. See the Terms and Conditions (https://onlinelibrary.wiley.com/terms-and-conditions) on Wiley Online Library for rules of use; OA articles are governed by the applicable Creative Commons License

2.2. Synthesis and Characterization of [BMPyrr][DCA]/UiO-66

The [BMPyrr][DCA]/UiO-66 composite was synthesized at a stoichiometric IL loading of 30 wt.% by using the wet impregnation method. After the synthesis of the composite, the first step was to validate the successful incorporation of the IL molecules into the MOF pores and to determine the corresponding IL loading. Thus, N_2 physisorption isotherms for pristine UiO-66 and IL-incorporated UiO-66 were acquired to confirm the successful incorporation of IL molecules into the MOF pores and its influence on the accessible surface area of UiO-66. Figure S4 (Supporting Information) shows that the N_2-adsorption isotherm of pristine MOF corresponds to the Type I isotherm, validating the existence of a microporous structure on UiO-66. Data further indicated that the pristine UiO-66 has a surface area and pore volume of 878 m^2 g^{-1} and 0.39 cm^3 g^{-1}, respectively. However, after the incorporation of [BMPyrr][DCA] into the UiO-66, the textural properties of the MOF deteriorated, and its surface area decreased to 7 m^2 g^{-1}. Such a substantial decrease in the surface area of IL-incorporated UiO-66 composite is expected due to the successful incorporation of the IL into the MOF nanocages.[6a,8b,15] On the contrary, the pore volume of the IL-incorporated MOF sample could not be determined. This can be attributed to two reasons: i) IL molecules might be occupying the pore openings of the MOF, obstructing the N_2 passage to access MOF pores at liquid nitrogen temperature, ii) N_2 has extremely poor solubility in [BMPyrr][DCA] at the measurement temperature, which may hinder the diffusion of N_2 through the channels blocked by the occupation of IL. Nonetheless, these observations are consistent with our previous reports.[6a,16]

To estimate the IL loading amount in the composite sample, we washed the sample using acetone as the solvent small enough to enter into the pores of MOF (≈8 Å) to remove the confined IL (≈7.4 Å from DFT calculations).[17] Thus, by washing the powder IL/UiO-66 composite with acetone, we were able to successfully remove the incorporated IL almost completely, as confirmed by FTIR analysis of the dry IL/UiO-66 composite before and after washing the sample with acetone, as shown in Figure S5 (Supporting Information). The corresponding IL loading in the composite was back-calculated based on the amount of IL removed from the [BMPyrr][DCA]/UiO-66 sample, which showed ≈22 wt.% of IL loading in the composite. Thus, we infer that the prepared IL/UiO-66 composite contains at least 22 wt.% of the confined IL. We note that this measured amount is slightly lower than the stoichiometric IL loading of 30 wt.% targeted to prepare [BMPyrr][DCA]/UiO-66 composite. This difference, as expected from the previous reports,[6a,18] can be attributed to the loss of some IL on the walls of the sample container during the synthesis process of the composite sample.

The crystalline structure of the UiO-66 before and after the incorporation of IL was examined using XRD analysis. Results shown in Figure S6a (Supporting Information) validate that the XRD pattern of UiO-66 is consistent with the previous studies reported in the literature.[14a] Furthermore, when [BMPyrr][DCA] was incorporated into the UiO-66, the key diffraction peaks of the MOF in the composite sample remained unchanged, implying that IL confinement has no significant effect on the crystallinity and structural stability of the parent MOF. Figure S6b (Supporting Information) shows the XRD pattern of simulated, pristine, and IL-incorporated UiO-66 structures. The crystalline structure of pristine UiO-66 has Fm3m symmetry with characteristic peaks at 7.34° for (111) and 8.47° for (200) reflections and with a unit cell parameter of 20.74 Å, in good agreement with the theoretical data.[19] After the incorporation of IL, the (111) and (200) peaks shift to lower 2θ values and the unit cell parameter increases to 20.91 Å, which could be as a result of the incorporation of IL molecules into the pores leading to an expansion in the unit cell of MOF structure. Besides, data further showed that the I_{111}/I_{200} peak ratio for the pristine MOF decreased from 4.35 to 3.43 upon the incorporation of IL. This change in the peak intensity ratios may suggest the modification of local electron density with the presence of IL molecules. In addition to these changes, the IL-incorporated MOF was further characterized by distinguished shoulder peaks next to the main characteristic peaks of the MOF. This result suggests that IL incorporation may modify the framework and result in the formation of new defect structures as evidenced by the formation of these shoulder peaks.

SEM images of the pristine MOF and its IL-incorporated counterpart were obtained to observe the morphologies, as demonstrated in Figure S7 (Supporting Information). It can be clearly observed that the crystal morphology and particle size of UiO-66 (Figure S7a, Supporting Information) remained well-preserved after the incorporation of the IL (Figure S7b, Supporting Information). As a result, we conclude that incorporating [BMPyrr][DCA] into UiO-66 had no adverse effect on the crystal morphology and particle size of the parent MOF. Additionally, it can also be observed that IL molecules have no influence on the surface morphology of the parent material, and no visible IL layer formation is observed in the SEM images, further indicating the confinement of IL molecules inside the pores of UiO-66. EDX analysis was performed on UiO-66 and IL/UiO-66 composite to determine their elemental composition. EDX spectra presented in Figure S8a (Supporting Information) indicate the presence of Zr, C, and O elements, corresponding to the elemental composition of UiO-66. On the contrary, EDX spectra of IL-incorporated UiO-66 given in Figure S8b (Supporting Information) show the presence of C, O, and Zr along with the elemental N. Since the N element only exists in bulk [BMPyrr][DCA], the appearance of elemental N in the EDX spectra of IL/UiO-66 composite further validates the successful incorporation of IL. Figure S8c (Supporting Information) depicts the elemental mapping images of the IL/UiO-66 composite, demonstrating the uniform distribution of elemental N, suggesting a homogenous dispersion of IL throughout the MOF in the composite sample.

To determine the thermal stability limits of IL/MOF composites, thermogravimetric analyses were performed on the bulk IL, pristine MOF, and IL/MOF composite under an inert atmosphere. **Figure 1** shows that pristine UiO-66 and bulk [BMPyrr][DCA] exhibited a single-step weight loss. The initial weight loss for each of the thermogravimetric plots in the temperature range of 100–200 °C can be associated with the volatilization of the adsorbed gases and water molecules, as well as the evaporation of any remaining solvent from the synthesis.

© 2022 The Authors. Advanced Functional Materials published by Wiley-VCH GmbH

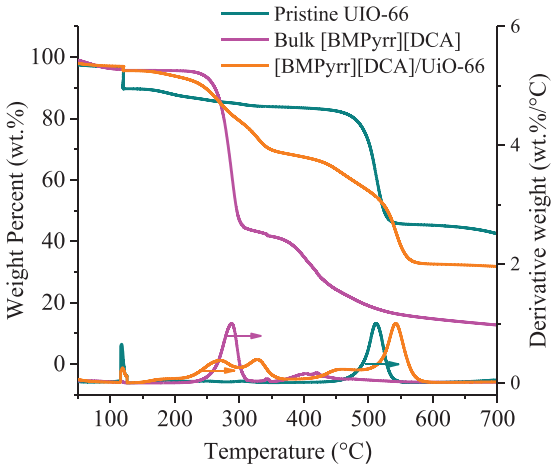


Figure 1. TGA and DTG curves of bulk [BMPyrr][DCA], UiO-66, and [BMPyrr][DCA]/UiO-66 composite.

According to the results presented in Figure 1, bulk [BMPyrr][DCA] and pristine UiO-66 demonstrate thermal stability up to T'_{onset} values of ≈258 and 480 °C, respectively. However, in the case of IL-incorporated UiO-66, T'_{onset} value decreased to 230 °C. This noticeable decrease in the thermal stability limit was presumably due to the confinement of IL into UiO-66 nanocages, accompanied by the formation of IL-MOF interactions, which alter the decomposition mechanism as evidenced by the TGA data showing a change from one-step to multiple-step decomposition (Figure 1).[20] These interactions cause a reduction in the thermal stability limits for the composite compared to the decomposition temperature of the pristine MOF or the bulk IL.

To seek better insights into the nature of these IL-MOF interactions, pristine UiO-66, bulk IL, and IL-incorporated UiO-66 were characterized by IR spectroscopy (**Figure 2**). Here, the comparison indicated that the IR spectrum of the IL/UiO-66 composite show new vibrational bands, which appear to be the characteristic peaks of the bulk IL, demonstrating the successful incorporation of IL into the UiO-66 framework. The easily recognizable bands in the lower region of IR spectra for pristine UiO-66 at 555, 742, 1393, and 1587 cm^{-1} are consistent with the literature. Among these, the bands at 555 and 742 cm^{-1} are assigned to the asymmetric Zr–(OC) and Zr–O modes stretching frequencies, whereas the two intense peaks at 1393 and 1587 cm^{-1} belong to the symmetric and asymmetric (O–C–O) stretching vibration in the carboxylate group, respectively.[14a,21] After the incorporation of IL into UiO-66 pores, these major IR bands exhibited shifts in their positions, indicating possible changes in the electronic environment of the MOF structure compared to pristine UiO-66. For instance, the peak at 555 cm^{-1} presented a red-shift of ≈12 cm^{-1}, while the other major peaks at 742, 1393, and 1587 cm^{-1} were blue-shifting to 749, 1396, and 1598 cm^{-1} upon the incorporation of the IL, respectively.[22] Meanwhile, the obvious strong IR bands at 1306, 2129, 2190, and 2230 cm^{-1} in the IR spectrum of the bulk IL are associated with the N≡C mode vibrations of the $[DCA]^-$ anion.[23] Moreover, those at 2875 and 2964 cm^{-1} are associated with the symmetric and asymmetric C–H

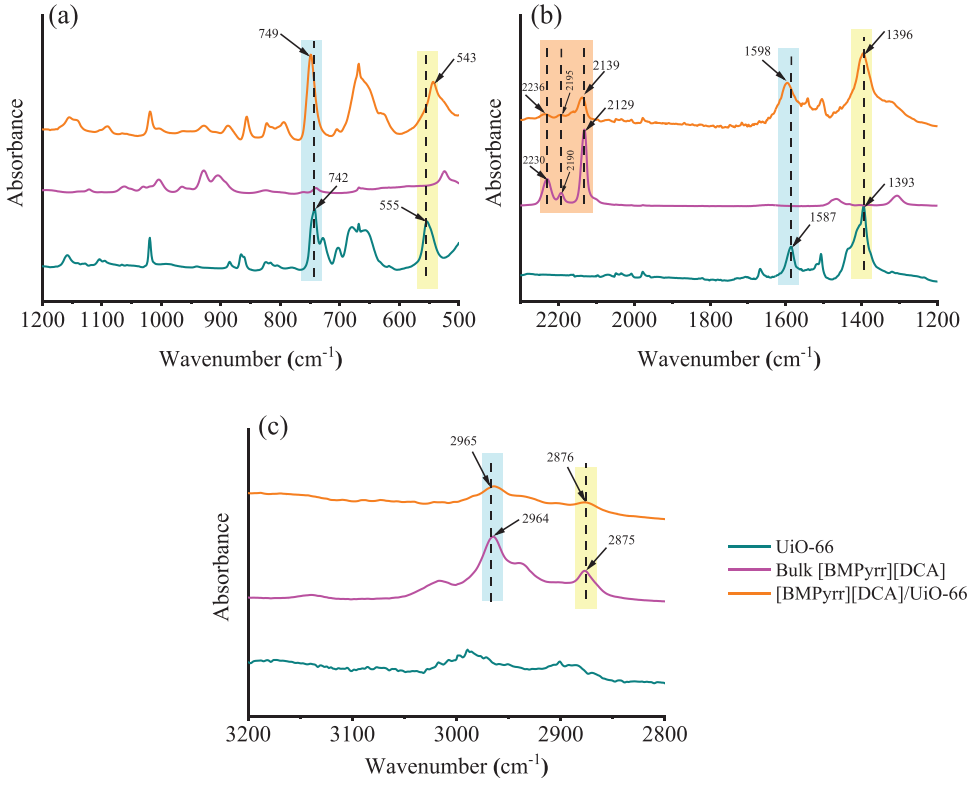


Figure 2. IR spectra of bulk [BMPyrr][DCA], pristine UiO-66, and [BMPyrr][DCA]/UiO-66; a) 1200–500 cm^{-1}, b) 2200–1200 cm^{-1}, and c) 3200–2800 cm^{-1}.

© 2022 The Authors. Advanced Functional Materials published by Wiley-VCH GmbH

16163028, 2022, 35, Downloaded from https://onlinelibrary.wiley.com/doi/10.1002/adfm.202204149 by Koc University, Wiley Online Library on [27/12/2022]. See the Terms and Conditions (https://onlinelibrary.wiley.com/terms-and-conditions) on Wiley Online Library for rules of use; OA articles are governed by the applicable Creative Commons License

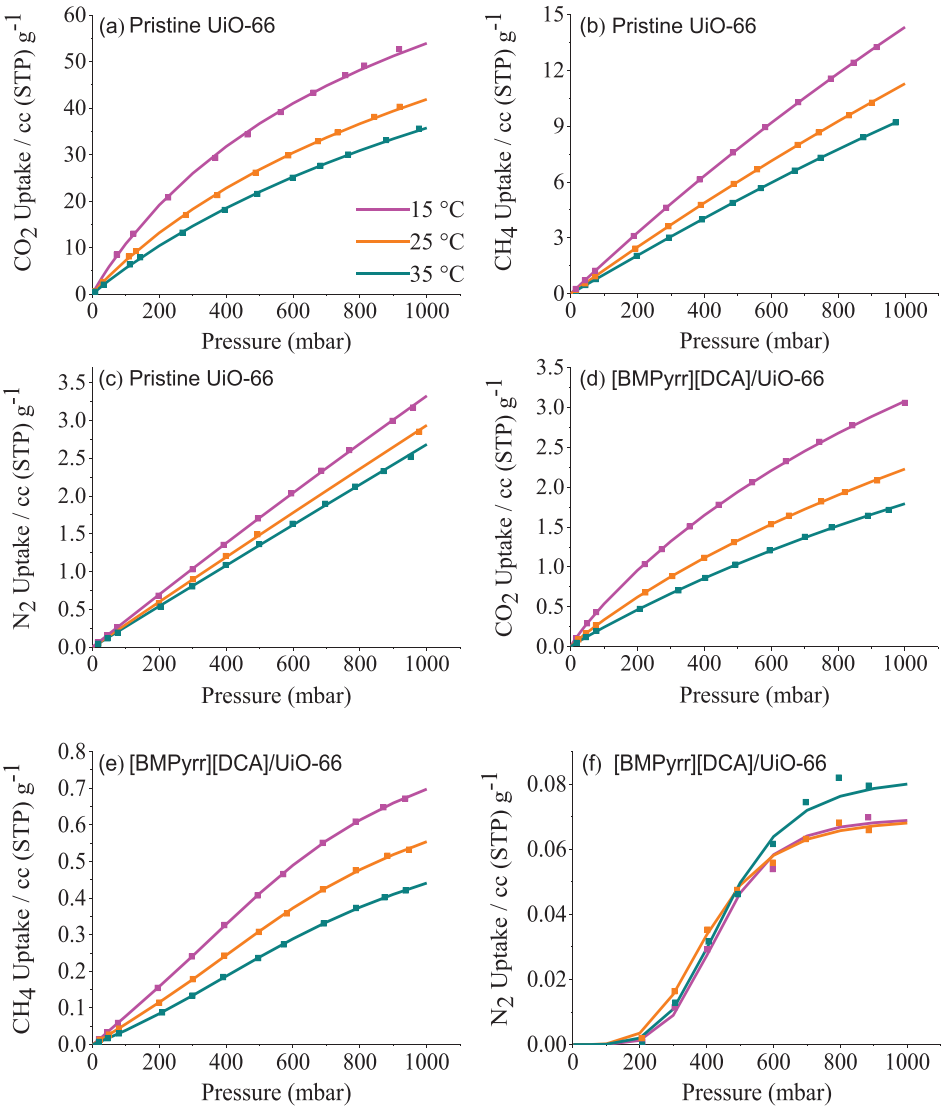


Figure 3. CO_2, CH_4, and N_2 uptakes of a–c) pristine UiO-66, d–f) [BMPyrr][DCA]/UiO-66 composite at 15, 25, and 35 °C up to 1000 mbar. Squares represent the experimental data and the straight lines represent the fitted data.

stretching vibrations of the IL cation. Hence, these shifts in the IR features associated with the MOF and the IL's anion verify the existence of interactions between the two moieties in the composite material. Zr–(OC) and Zr–O stretching vibration of the metal nodes of the MOF exhibited significant shifts compared to the changes in the band positions correlated to the carboxylate group, which suggests that the IL's anion strongly interacts with Zr metal nodes of the MOF. The direct interactions between [BMPyrr][DCA] and UiO-66 were also confirmed at the atomic level by DFT calculations, and the shifts in vibrational bands of ν(N≡C) were further validated by frequency calculations as given in Table S4 (Supporting Information). In the DFT-level optimized ground state geometry of [BMPyrr][DCA]/UiO-66 cluster model composite, the anion is in close contact with the Zr node (with the central N of $[DCA]^-$ is at a distance of 4.71 Å), as represented in Figure S9 (Supporting Information).

2.3. Gas Adsorption and Separation with [BMPyrr][DCA]/UiO-66

To assess the influence of [BMPyrr][DCA] incorporation on the CO_2/N_2, CO_2/CH_4, and CH_4/N_2 separation performances of the UiO-66, volumetric CO_2, N_2, and CH_4 adsorption isotherms were measured. Accordingly, the measurements were conducted at three different temperatures (15, 25, and 35 °C) in a pressure range of 1–1000 mbar. **Figure 3** shows the fitted data of experimental CO_2, N_2, and CH_4 adsorption isotherms for pristine UiO-66 and [BMPyrr][DCA]/UiO-66 composite. As expected, with the increase in temperature from 15 to 35 °C, the gas adsorption capacities of both UiO-66 and its composite decreased. CO_2, N_2, and CH_4 uptakes (Figure 3d–f) of [BMPyrr][DCA]/UiO-66 composite were drastically lower than those of pristine UiO-66. This result is expected as the successful confinement of IL into UiO-66 reduces the overall available surface area and pore volume of the MOF, as evidenced by the BET

© 2022 The Authors. Advanced Functional Materials published by Wiley-VCH GmbH

16163028, 2022, 35, Downloaded from https://onlinelibrary.wiley.com/doi/10.1002/adfm.202204149 by Koc University, Wiley Online Library on [27/12/2022]. See the Terms and Conditions (https://onlinelibrary.wiley.com/terms-and-conditions) on Wiley Online Library for rules of use; OA articles are governed by the applicable Creative Commons License

16163028, 2022, 35, Downloaded from https://onlinelibrary.wiley.com/doi/10.1002/adfm.202204149 by Koc University, Wiley Online Library on [27/12/2022]. See the Terms and Conditions (https://onlinelibrary.wiley.com/terms-and-conditions) on Wiley Online Library for rules of use; OA articles are governed by the applicable Creative Commons License

results of the composite. However, it is important to mention that the composite exhibited significantly poor CH_4 adsorption and almost no N_2 adsorption in the low-pressure range. The difference in the level of decreases in the gas uptakes is governed by the acidic nature of CO_2 molecules, which has a strong affinity towards the highly basic anion ($[DCA]^-$) of the IL confined in nanocages of UiO-66 compared to N_2 and CH_4 molecules.

This synergistic Lewis acid/base and van der Waals interactions between the CO_2 molecules and IL were further validated by DFT and COSMO-RS calculations. The 3D representations of the equilibrium geometries of IL-gas pairs are presented in Figure S3 (Supporting Information). When CO_2 makes a stable complex with the IL, positively charged C of CO_2 ($q_C = 1.025e$) forms the Lewis acid-base interaction with negatively charged N-heteroatom of $[DCA]^-$ ($q_N = -0.581e$), and additional H-bond formed between negatively charged O of CO_2 ($q_O = -0.549e$) and one of the hydrogens on the pyrrolidinium ring strengthens the adsorption of CO_2 with the calculated binding energy of 24.4 kJ mol^{-1}, as represented in Figure S3a (Supporting Information). CH_4 is also primarily adsorbed by the anion with a BE of 10.1 kJ mol^{-1} through the weak hydrogen bonding formed between CH_4 and N-heteroatom of $[DCA]^-$ as shown in Figure S3b (Supporting Information). Figure S3c (Supporting Information) illustrates that N_2 mostly interacts with the cation with a very low BE of 7.9 kJ mol^{-1}. These findings point out that [BMPyrr][DCA] has a high affinity toward CO_2 and a low affinity for CH_4 and N_2 gases. Moreover, Figure S10 (Supporting Information), which is obtained from COSMO-RS calculations, demonstrates that CO_2 has significantly higher solubility in [BMPyrr][DCA] compared to almost negligible N_2 and CH_4 solubilities. In addition, the presence of confined IL moieties in the composite facilitates the diffusion of CO_2 through the blocked pores due to its high solubility and interaction strength with the IL. In contrast, the confined IL moieties limit the ability of N_2 and CH_4 molecules to diffuse through the blocked microporous channels of the composite. Consequently, CO_2 uptake in IL-incorporated MOF is significantly higher than N_2 and CH_4 uptakes in the composite.

Next, we repeated the gas adsorption measurements on the used sample to demonstrate the reusability of the composite material and reproducibility of uptake data. Figure S11 (Supporting Information) indicates that the composite material is reusable, and uptake data are reproducible within an error range of ≤±5%.

A comparison of the experimental and simulated gas uptakes of [BMPyrr][DCA]/UiO-66 composite between 100 and 1000 mbar at 25 °C is provided in Figure S12a (Supporting Information). The presence of crystal defects and inaccessible adsorption sites in the MOF structure may significantly affect the gas adsorption results. Since these effects are not considered in molecular simulations, scaling factors were applied to the simulated gas uptakes of the composites to compensate for systematic deviations as described in previous reports.[24] Thus, the gas uptakes obtained from GCMC simulations were multiplied by a pressure-dependent scaling factor defined previously on similar IL/MOF composites[8b] to improve the agreement between simulations and experiments. Here, we note that the N_2 uptake values measured experimentally for the composite are very low, <0.1 cc g^{-1}, and that those obtained from GCMC simulations overestimate these experimental values at especially low pressures, at which the N_2 uptake values are almost becoming lower than the measurable limits (Figure S12a, Supporting Information). This difference between experimental and simulation results indicates that the scaling factor used to correct the GCMC values becomes insufficient when the uptake values are exceptionally low. Figure S12b (Supporting Information) compares the experimental and simulated (and scaled) gas uptake values obtained on different IL/MOF composites and demonstrates that even though the GCMC results overestimate the experimental values on the [BMPyrr][DCA]/UiO-66, they remain orders of magnitude lower, <0.1 cc g^{-1}, compared to those of other composites. Hence, we infer that the agreement between experiments and simulations is reasonable and that our calculations/simulations could successfully identify the top performing IL/UiO-66 composite.

It is of great interest to evaluate CO_2/N_2, CO_2/CH_4, and CH_4/N_2 selectivities of the composite sample, since it offers substantially poor uptakes for N_2 and CH_4 compared to CO_2. To compare the gas separation performance of pristine UiO-66 and IL-incorporated UiO-66, single-component CO_2, N_2, and CH_4 adsorption isotherms obtained at 15, 25, and 35 °C were fitted to Langmuir-Freundlich, dual-site Langmuir, and dual-site Langmuir–Freundlich models. Accordingly, ideal CO_2/N_2, CO_2/CH_4, and CH_4/N_2 selectivities were calculated in the pressure range of 1–1000 mbar at 15, 25, and 35 °C, as shown in **Figure 4**. At 1 mbar, ideal CO_2/N_2, CO_2/CH_4, and CH_4/N_2 selectivities were computed as 44.1, 9.1, and 4.8 for pristine UiO-66 at 15 °C. Reduced selectivities were reported with increasing temperatures: 33.8, 7.8, and 4.3 at 25 °C and 26.2, 6.7, and 3.9 at 35 °C, respectively. Moreover, as the pressure increases from 1 to 1000 mbar, the ideal selectivities tend to decrease and almost become half of their values at 1000 mbar compared to 1 mbar. This result is expected because the gas separation performance of a material at relatively higher pressure is governed by the available pore volume, as opposed to the gas separation performance at low pressure when interactions between the guest molecules and adsorbent are significant.[3a]

Upon the incorporation of IL into UiO-66 cages, the CO_2 separation performance was substantially improved. At 1000 mbar, the [BMPyrr][DCA]/UiO-66 composite presented approximately three times higher ideal CO_2/N_2 selectivity compared to that of pristine UiO-66. Notably, an extraordinary improvement in the ideal CO_2/N_2 selectivity was recorded for the [BMPyrr][DCA]/UiO-66 composite at 15 °C and 100 mbar, boosting from 31 to 14 106, corresponding to an ≈455 times improvement (Figure 4b) in CO_2 separation performance. Moreover, in the low-pressure region (1–50 mbar), the ideal CO_2/N_2 selectivity increased from 44 at 15 °C (33.8 at 25 °C and 26.2 at 35 °C) to almost infinite selectivity (>100 000), (Figure 4a). Similarly, in the low-pressure region, the ideal CH_4/N_2 selectivity of IL/UiO-66 composite approaches to practically infinite (Figure 4c), whereas the corresponding selectivity boosted 436 times at 100 mbar and 15 °C (Figure 4d). In addition to these, the ideal CO_2/CH_4 selectivity showed a two times improvement (Figure 4e) at 1 mbar upon the incorporation of [BMPyrr][DCA] into UiO-66. ILs with cyano groups either in their cation or anion parts offer excellent CO_2-phillic characteristics, which is also validated by the COSMO-RS

© 2022 The Authors. Advanced Functional Materials published by Wiley-VCH GmbH

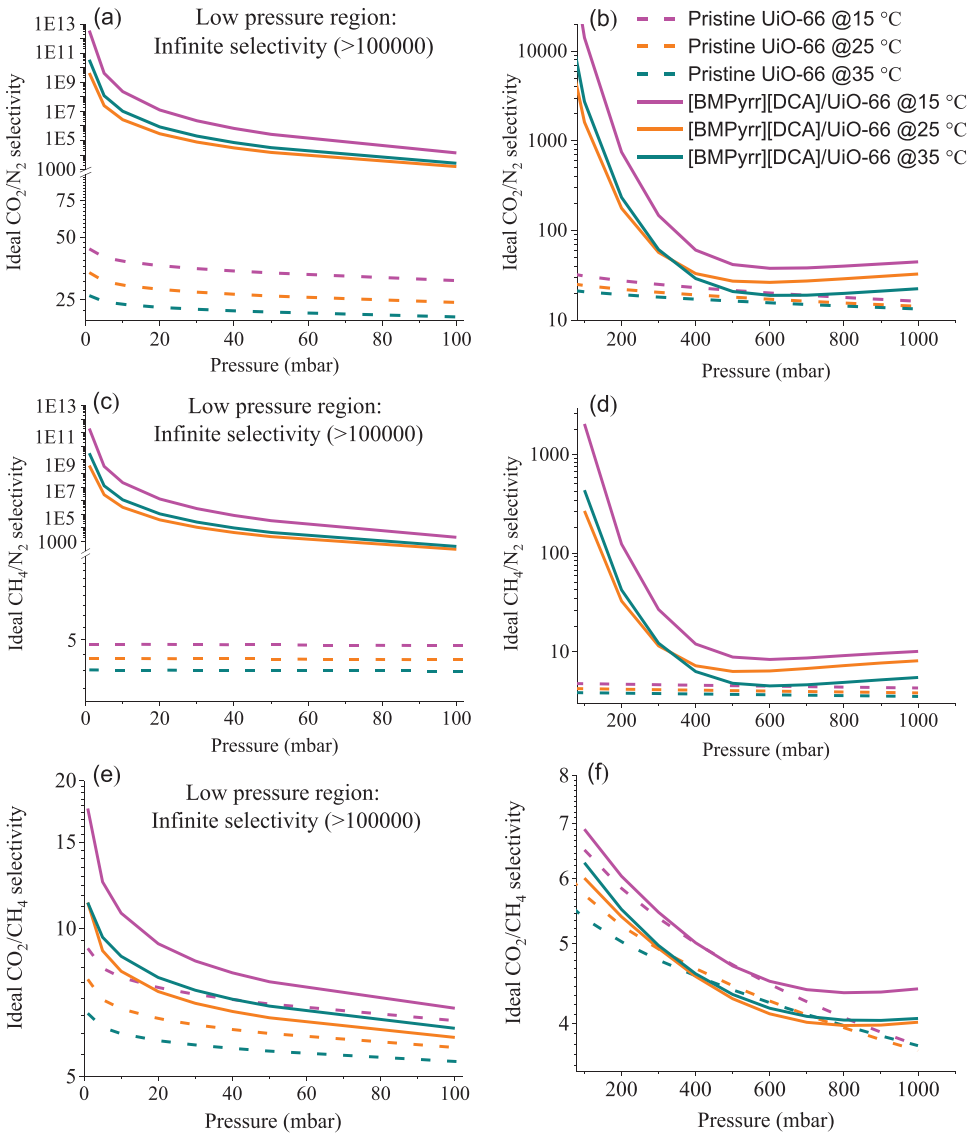


Figure 4. a,b) CO_2/N_2, c,d) CH_4/N_2, e,f) CO_2/CH_4 ideal selectivities of pristine UiO-66 and [BMPyrr][DCA]/UiO-66 composite at 15, 25, and 35 °C. Ideal selectivities on the *y*-axis are given in a logarithmic scale, and the curves are given to guide the eye.

and the DFT results.[25] Therefore, this extraordinary improvement in CO_2 separation performance can be rationalized by the superior solubility and the presence of synergistic interactions between CO_2 molecules and the confined IL, which facilitate the diffusion of CO_2 molecules. Meanwhile, extremely poor solubilities of N_2 and CH_4 in [BMPyrr][DCA] offer a CH_4- and N_2-phobic environment in the MOF pores, posing a significant hindrance for the adsorption of CH_4 and N_2 molecules accompanied by a significantly improved CO_2 separation performance. To the best of our knowledge, these results are the highest ideal CO_2/N_2 selectivities achieved among all the post-synthetically IL-functionalized MOF composites reported to date. Because the flue gas from power plants contains a substantial amount of N_2, the development of a new adsorbent material with superior CO_2/N_2 selectivity is critical. Likewise, in the case of natural gas processing plants, the separation of excess N_2 from CH_4 containing streams is extremely important for plant efficiency. Thus, we believe that the rational design of [BMPyrr][DCA]/UiO-66 composite with practically infinite CO_2/N_2 and CH_4/N_2 selectivities offers an excellent opportunity for post-combustion CO_2 capture applications.

3. Conclusion

In this work, we present an integrated computational–experimental hierarchical approach to systematically choose an IL to design a novel IL/MOF composite with exceptional CO_2 selectivity. We first used COSMO-RS calculations to screen 1488 different pyrrolidinium-based ILs and systematically identified the most promising ILs by employing several structure and performance filters. We then generated 27 IL/UiO-66 composites by incorporating each DFT-optimized IL into UiO-66 and performed GCMC simulations to compute the corresponding CO_2,

© 2022 The Authors. Advanced Functional Materials published by Wiley-VCH GmbH

16163028, 2022, 35, Downloaded from https://onlinelibrary.wiley.com/doi/10.1002/adfm.202204149 by Koc University, Wiley Online Library on [27/12/2022]. See the Terms and Conditions (https://onlinelibrary.wiley.com/terms-and-conditions) on Wiley Online Library for rules of use; OA articles are governed by the applicable Creative Commons License

N_2, and CH_4 uptakes in these composites. Among the composites considered, [BMPyrr][DCA]/UiO-66 was identified as the one offering the highest CO_2 separation performance. Next, it was synthesized and characterized in deep detail. The gas adsorption experiments showed that [BMPyrr][DCA]/UiO-66 composite offers extraordinarily high ideal CO_2/N_2 and CH_4/N_2 selectivities. Notably, in the low-pressure region, the CO_2 selectivity becomes practically infinite (>100 000) at 15, 25, and 35 °C. In addition, the ideal CO_2/N_2 and CH_4/N_2 selectivities of IL/UiO-66 composite improved by 455 and 430 times compared to the corresponding ideal selectivities of pristine UiO-66 at 100 mbar and 15 °C, respectively. This work demonstrates that synergistic interactions between IL-MOF moieties and a rational choice of IL-MOF combination are imperative to create a novel composite with extraordinary CO_2 separation performance. We believe that this multi-level computational approach to design the best IL-MOF candidates and experimental assessment of the novel composite materials can potentially offer a broad potential for the design of new composites with exceptional performance for any target application.

4. Experimental Section

Part A: Computational: Ionic liquid screening module in COSMO-RS was used to quickly screen large datasets of ILs and to identify the promising ILs with the highest CO_2 solubility.[26] COSMO-RS is an efficient and widely used computational modeling tool to estimate the solubilities of various gases in bulk ILs qualitatively.[27] The gas solubilities in ILs were estimated from the activity coefficients at infinite dilution using the equation below.

$$C_{i,j}^{\infty} = \frac{1}{\gamma_{i,j}} \quad (1)$$

Here, $C_{i,j}^{\infty}$ and $\gamma_{i,j}$ represent gas solubility and activity coefficient for component *i* in the IL *j* at infinite dilution. Gas solubilities of the top performing bulk ILs were obtained at 25 °C in a pressure range of 100–1000 mbar. These calculations were carried out using TZVP parameterization in COSMOThermX software, version C30_160.

Twenty-seven IL structures were optimized by employing Becke-three-parameter-Lee-Yang-Parr (B3LYP) functional including Grimme's D2 correction and 6–311++G** basis set using the Gaussian09 program.[28] The binding energies between the gases and [BMPyrr][DCA] were calculated by using,

$$\Delta E_{bind} = E_{IL+Gas} - (E_{IL} + E_{Gas}) + \Delta E^{ZPE} + \delta^{BSSE} \quad (2)$$

where E_{IL+Gas} is the optimized energy of the IL-gas complex, E_{IL} and E_{Gas} denote the optimized energies of IL and gas molecule, ΔE^{ZPE} is the zero-point energy correction, and δ^{BSSE} is the basis set superposition error correction employed by the Counter Poise approach. Natural Bond Orbital (NBO) analyses were performed to understand the nature of the electrostatic interactions between the IL and the gases.[29] The optimization of the cluster model of the selected IL/UIO-66 composite was performed at B3LYP-D2/6-31G* level of theory, and the vibrational frequencies were calculated at the same level, which were scaled by a factor of 0.9614[30] to compensate for harmonic effects.

To incorporate ILs into UiO-66, the Baker's minimization approach[31] in the NVT ensemble (constant number of particles (N), volume (V), and temperature (T)) was employed, as implemented in the RASPA simulation code.[32] During minimization, IL molecules were allowed to freely move inside the MOF cage. A minimum energy configuration with all positive eigenvalues in the Hessian matrix was obtained using Baker's minimization.[33] The energy minimization procedure was continued until the root-mean-square (RMS) gradient tolerance and maximum gradient tolerance were $\leq 10^{-6}$. The RMS gradient tolerance was the maximum allowed RMS gradient calculated by using the energy gradient difference between two iterations, and the maximum gradient tolerance was the maximum allowed gradient for each atom. Additional information on the optimization and minimization procedures for the IL-incorporated UiO-66 composites were described in the previous study.[8b] The IL loading was set to ≈25 wt.%, close to the experimentally reported value. The RASPA simulation code version 2.0.37 was used to conduct the GCMC simulations.[32] The non-bonded interactions were defined using the Lennard–Jones (LJ) potential, and the cut-off distance for interatomic interactions was set to 13 Å. The potential parameters for the IL and MOF atoms were obtained from the DREIDING force field, except for the zirconium atom, for which the parameters were acquired from the Universal Force Field (UFF).[34] A three-site rigid molecule with LJ 12–6 potential was used to represent CO_2 with partial charges at the center of each site.[35] N_2 was modeled as a three-site rigid molecule with N atoms at two sites and a center of mass with partial point charges at the third site.[36] A single site sphere with LJ 12–6 potential was used to model CH_4.[37] The charge equilibration method (*Q*eq) was used to assign partial charges to MOF and IL atoms.[38] Single component GCMC simulations for CO_2, N_2, and CH_4 adsorption were performed between 100 and 1000 mbar at 25 °C. The total number of cycles was set to 30 000, with the first 10 000 cycles used to initialize the system and the last 20 000 cycles used to take ensemble averages. The isosteric heats of adsorption (ΔQ_{st}) values for gases were computed using the fluctuations in the potential energy of the system during the GCMC simulations.[39]

Part B: Experimental: UiO-66 (ACSYNAM, Canada), [BMPyrr][DCA] (Iolitec, >98%), and acetone (Sigma–Aldrich, ≥99.5%) were kept in Ar-filled glove box (Labconco) and used as received. To prepare 30 wt.% IL-incorporated UiO-66 sample, [BMPyrr][DCA] (0.3 g) was first dissolved in acetone (20 mL). The solution was stirred at room temperature until a homogenous solution was obtained. Next, 0.6 g of dehydrated UiO-66 powder dried overnight under vacuum at 125 °C was added to the homogeneous solution. Subsequently, the mixture was kept at 35 °C and continuously stirred for 6 h to gradually evaporate the solvent. Finally, the product was further dried overnight at 105 °C to remove any remaining solvent molecules.

XRD analysis for UiO-66 and [BMPyrr][DCA]/UiO-66 composite were recorded on a Bruker D8 Advance using Cu-Kα1 radiation source. Each spectrum was obtained in the 2θ range of 5–50° by employing a scan step size of 0.02°. Surface morphologies were assessed under ultra-high vacuum on a Zeiss Evo LS 15 electron microscope, and each sample was coated with gold prior to the analysis. EDX analysis and elemental mapping of the samples were performed on a Bruker XFlash 5010 EDX detector operating at 5 kV. The working distance was set to 5.6 mm for each analysis. The XRD profile fitting was performed on the pristine and IL incorporated MOF structures using the pseudo-Voigt function using the TOPAS 4.2 software.

N_2 adsorption–desorption isotherms were obtained on a Micromeritics ASAP 2020 at −196 °C to determine BET surface area and pore volume of the samples. Before the analysis, each sample was degassed for 12 h at 125 °C under high vacuum. The corresponding BET surface area was calculated by fitting the BET equation in a relative pressure range of 0.05–1 bar, whereas the pore volume of the samples was determined using the *t*-plot method.

TG analysis was carried out on a TA Instruments Q500 thermogravimetric analyzer. Each experiment was conducted according to the previously reported procedure.[20,40] To compare the thermal stabilities of the samples, derivative onset (T'_{onset}) temperatures calculated from the derivative gravimetric (DTG) curves were considered as the decomposition temperatures in this study. IR spectra of samples was recorded in absorption mode on a Bruker Vertex 80v IR spectrometer in the IR frequency range of 3200–500 cm^{-1} and at a scanning resolution of 2 cm^{-1}. Each sample spectrum was obtained by averaging 256 scans. Finally, the Voigt function was employed with Fityk software to deconvolute and fit the peaks.[41]

© 2022 The Authors. Advanced Functional Materials published by Wiley-VCH GmbH

16163028, 2022, 35, Downloaded from https://onlinelibrary.wiley.com/doi/10.1002/adfm.202204149 by Koc University, Wiley Online Library on [27/12/2022]. See the Terms and Conditions (https://onlinelibrary.wiley.com/terms-and-conditions) on Wiley Online Library for rules of use; OA articles are governed by the applicable Creative Commons License

CH_4, CO_2, and N_2 adsorption isotherms for UiO-66 and IL-incorporated UiO-66 were collected on a volumetric gas sorption analyzer, iSorb HP2, Quantachrome. Adsorption isotherms for each sample were collected at three different temperatures (15, 25, and 35 °C) in a pressure range of 10–1000 mbar, respectively. Before each gas adsorption analysis, samples were degassed at 125 °C under a high vacuum for ≈12 h. To compare the gas separation performance of pristine UiO-66 with IL/UiO-66 composite, adsorption isotherms were fitted to Langmuir–Freundlich (LF), dual-site Langmuir (DSL), and dual-site Langmuir–Freundlich (DSLF) models. All these model fittings were performed using Ideal Adsorbed Solution Theory (IAST)$^{++}$ software.[42]

Supporting Information

Supporting Information is available from the Wiley Online Library or from the author.

Acknowledgements

M.Z., H.C.G., and O.D. contributed equally to this work. This work received funding from the Scientific and Technological Research Council of Turkey (TUBITAK) under 1001-Scientific and Technological Research Projects Funding Program (Project Number 114R093). S.K. acknowledges ERC-2017-Starting Grant. This study was funded by the European Research Council (ERC) under the European Union's Horizon 2020 research and innovation programme (ERC-2017-Starting Grant, grant agreement no. 756489-COSMOS). The authors thank to the support of Koç University TÜPRAŞ Energy Center (KUTEM) and Koç University Surface Science and Technology Center (KUYTAM). M.Z. acknowledges HEC Pakistan Scholarship.

Conflict of Interest

The authors declare no conflict of interest.

Data Availability Statement

The data that support the findings of this study are available in the supplementary material of this article.

Keywords

density functional theory (DFT), gas separation, ionic liquids (ILs), metal–organic frameworks (MOFs), molecular simulations

Received: April 13, 2022
Revised: May 25, 2022
Published online: June 26, 2022

[1] a) A. J. Howarth, Y. Liu, P. Li, Z. Li, T. C. Wang, J. T. Hupp, O. K. Farha, *Nat. Rev. Mater.* **2016**, *1*, 15018; b) Z. Shi, Y. Tao, J. Wu, C. Zhang, H. He, L. Long, Y. Lee, T. Li, Y.-B. Zhang, *J. Am. Chem. Soc.* **2020**, *142*, 2750.

[2] a) P. G. Jessop, T. Ikariya, R. Noyori, *Chem. Rev.* **1999**, *99*, 475; b) B. E. Gurkan, J. C. de la Fuente, E. M. Mindrup, L. E. Ficke, B. F. Goodrich, E. A. Price, W. F. Schneider, J. F. Brennecke, *J. Am. Chem. Soc.* **2010**, *132*, 2116.

[3] a) F. P. Kinik, A. Uzun, S. Keskin, *ChemSusChem* **2017**, *10*, 2842; b) Ö. Durak, M. Zeeshan, N. Habib, H. C. Gulbalkan, A. A. A. M. Alsuhile, H. P. Çağlayan, S. F. Kurtoğlu-Öztulum, Y. Zhao, Z. P. Haşlak, A. Uzun, *Microporous Mesoporous Mater.* **2022**, 111703.

[4] a) M. Zeeshan, V. Nozari, M. B. Yagci, T. Isık, U. Unal, V. Ortalan, S. Keskin, A. Uzun, *J. Am. Chem. Soc.* **2018**, *140*, 10113; b) M. Mohamedali, H. Ibrahim, A. Henni, *Chem. Eng. J.* **2018**, *334*, 817.

[5] F. P. Kinik, C. Altintas, V. Balci, B. Koyuturk, A. Uzun, S. Keskin, *ACS Appl. Mater. Interfaces* **2016**, *8*, 30992.

[6] a) M. Zeeshan, H. Kulak, S. Kavak, H. M. Polat, O. Durak, S. Keskin, A. Uzun, *Microporous Mesoporous Mater.* **2020**, *306*, 110446; b) M. Mohamedali, A. Henni, H. Ibrahim, *Microporous Mesoporous Mater.* **2019**, *284*, 98.

[7] a) M. Ding, H.-L. Jiang, *ACS Catal.* **2018**, *8*, 3194; b) W.-L. Xue, L. Wang, Y. K. Li, H. Chen, K. X. Fu, F. Zhang, T. He, Y. H. Deng, J. R. Li, C.-Q. Wan, *ACS Sustainable Chem. Eng.* **2020**, *8*, 18558.

[8] a) B. Koyuturk, C. Altintas, F. P. Kinik, S. Keskin, A. Uzun, *J. Phys. Chem. C* **2017**, *121*, 10370; b) H. M. Polat, M. Zeeshan, A. Uzun, S. Keskin, *Chem. Eng. J.* **2019**, *373*, 1179; c) N. A. Khan, Z. Hasan, S. H. Jhung, *Chem. Commun.* **2016**, *52*, 2561.

[9] M. Usman, A. Helal, M. M. Abdelnaby, A. M. Alloush, M. Zeama, Z. H. Yamani, *Chem. Rec.* **2021**, *21*, 1771.

[10] A. H. Vahabi, F. Norouzi, E. Sheibani, M. Rahimi-Nasrabadi, *Coord. Chem. Rev.* **2021**, *445*, 214050.

[11] H. Demir, S. Keskin, *J. CO_2 Util.* **2022**, *55*, 101811.

[12] a) A. Thomas, R. Ahamed, M. Prakash, *RSC Adv.* **2020**, *10*, 39160; b) J. Praus, P. Pokorný, P. Číhal, O. Vopička, *Fluid Phase Equilib.* **2022**, *557*, 113418; c) M. N. Jorabchi, R. Ludwig, D. Paschek, *J. Phys. Chem. B* **2021**, *125*, 1647.

[13] Z. Salleh, I. Wazeer, S. Mulyono, L. El-blidi, M. A. Hashim, M. K. Hadj-Kali, *J. Chem. Thermodyn.* **2017**, *104*, 33.

[14] a) Ö. Durak, H. Kulak, S. Kavak, H. M. Polat, S. Keskin, A. Uzun, *J. Phys.: Condens. Matter* **2020**, *32*, 484001; b) T. J. Ferreira, R. P. Ribeiro, J. P. Mota, L. P. Rebelo, J. M. Esperança, I. A. Esteves, *ACS Appl. Nano Mater.* **2019**, *2*, 7933.

[15] V. Nozari, S. Keskin, A. Uzun, *ACS Omega* **2017**, *2*, 6613.

[16] M. Zeeshan, H. C. Gulbalkan, Z. P. Haslak, S. Keskin, A. Uzun, *Microporous Mesoporous Mater.* **2021**, *316*, 110947.

[17] P. Iacomi, U.-H. Lee, A. H. Valekar, J.-S. Chang, P. L. Llewellyn, *RSC Adv.* **2019**, *9*, 7128.

[18] K. B. Sezginel, S. Keskin, A. Uzun, *Langmuir* **2016**, *32*, 1139.

[19] S. Øien, D. Wragg, H. Reinsch, S. Svelle, S. Bordiga, C. Lamberti, K. P. Lillerud, *Cryst. Growth Des.* **2014**, *14*, 5370.

[20] M. Zeeshan, V. Nozari, S. Keskin, A. Uzun, *Ind. Eng. Chem. Res.* **2019**, *58*, 14124.

[21] Z. Jin, H. Yang, *Nanoscale Res. Lett.* **2017**, *12*, 5.

[22] Y. Cao, Y. Zhao, Z. Lv, F. Song, Q. Zhong, *J. Ind. Eng. Chem.* **2015**, *27*, 102.

[23] O. Palumbo, F. Trequattrini, J.-B. Brubach, P. Roy, A. Paolone, *Appl. Sci.* **2020**, *10*, 4837.

[24] a) Y.-S. Bae, K. L. Mulfort, H. Frost, P. Ryan, S. Punnathanam, L. J. Broadbelt, J. T. Hupp, R. Q. Snurr, *Langmuir* **2008**, *24*, 8592; b) D. Dubbeldam, H. Frost, K. S. Walton, R. Q. Snurr, *Fluid Phase Equilib.* **2007**, *261*, 152.

[25] a) M. J. Muldoon, S. N. Aki, J. L. Anderson, J. K. Dixon, J. F. Brennecke, *J. Phys. Chem. B* **2007**, *111*, 9001; b) L. C. Tomé, M. Isik, C. S. Freire, D. Mecerreyes, I. M. Marrucho, *J. Membr. Sci.* **2015**, *483*, 155.

[26] a) COSMOtherm, http://www.cosmologic.de/http://www.cosmologic.de/ (accessed: July 2021); b) R. Anantharaj, T. Banerjee, *Ind. Eng. Chem. Res.* **2010**, *49*, 8705; c) Y. S. Sistla, A. Khanna, *J. Chem. Eng. Data* **2011**, *56*, 4045.

[27] S. Gao, X. Chen, R. Abro, A. A. Abdeltawab, S. S. Al-Deyab, G. Yu, *Ind. Eng. Chem. Res.* **2015**, *54*, 9421.

[28] a) A. D. Becke, *J. Chem. Phys.* **1992**, *96*, 2155; b) C. Lee, W. Yang, R. G. Parr, *Phys. Rev. B* **1988**, *37*, 785; c) S. Grimme, J. Antony,

© 2022 The Authors. Advanced Functional Materials published by Wiley-VCH GmbH

16163028, 2022, 35, Downloaded from https://onlinelibrary.wiley.com/doi/10.1002/adfm.202204149 by Koc University, Wiley Online Library on [27/12/2022]. See the Terms and Conditions (https://onlinelibrary.wiley.com/terms-and-conditions) on Wiley Online Library for rules of use; OA articles are governed by the applicable Creative Commons License

S. Ehrlich, H. Krieg, *J. Chem. Phys.* **2010**, *132*, 154104; d) N. Godbout, D. R. Salahub, J. Andzelm, E. Wimmer, *Can. J. Chem.* **1992**, *70*, 560.
[29] A. E. Reed, R. B. Weinstock, F. Weinhold, *J. Chem. Phys.* **1985**, *83*, 735.
[30] J. P. Merrick, D. Moran, L. Radom, *J. Phys. Chem. A* **2007**, *111*, 11683.
[31] J. Baker, *J. Comput. Chem.* **1986**, *7*, 385.
[32] D. Dubbeldam, S. Calero, D. E. Ellis, R. Q. Snurr, *Mol. Simul.* **2016**, *42*, 81.
[33] D. Dubbeldam, R. Krishna, R. Q. Snurr, *J. Phys. Chem. C* **2009**, *113*, 19317.
[34] a) S. L. Mayo, B. D. Olafson, W. A. Goddard, *J. Phys. Chem.* **1990**, *94*, 8897; b) A. K. Rappé, C. J. Casewit, K. Colwell, W. A. Goddard III, W. M. Skiff, *J. Am. Chem. Soc.* **1992**, *114*, 10024.
[35] J. J. Potoff, J. I. Siepmann, *AIChE J.* **2001**, *47*, 1676.
[36] C. Murthy, K. Singer, M. Klein, I. McDonald, *Mol. Phys.* **1980**, *41*, 1387.
[37] M. G. Martin, J. I. Siepmann, *J. Phys. Chem. B* **1998**, *102*, 2569.
[38] a) A. K. Rappe, W. A. GoddardIII, *J. Phys. Chem.* **1991**, *95*, 3358; b) C. E. Wilmer, R. Q. Snurr, *Chem. Eng. J.* **2011**, *171*, 775.
[39] T. Vlugt, E. García-Pérez, D. Dubbeldam, S. Ban, S. Calero, *J. Chem. Theory Comput.* **2008**, *4*, 1107.
[40] M. Babucci, Akçay, A. , Balci, V. , Uzun, A. , *Langmuir* **2015**, *31*, 9163.
[41] M. Wojdyr, *J. Appl. Crystallogr.* **2010**, *43*, 1126.
[42] S. Lee, J. H. Lee, J. Kim, *Korean J. Chem. Eng.* **2018**, *35*, 214.

© 2022 The Authors. Advanced Functional Materials published by Wiley-VCH GmbH

16163028, 2022, 35, Downloaded from https://onlinelibrary.wiley.com/doi/10.1002/adfm.202204149 by Koc University, Wiley Online Library on [27/12/2022]. See the Terms and Conditions (https://onlinelibrary.wiley.com/terms-and-conditions) on Wiley Online Library for rules of use; OA articles are governed by the applicable Creative Commons License